

Complex Dispersion of Detonation Nanodiamond Revealed by Machine Learning Assisted Cryo-TEM and Coarse-Grained Molecular Dynamics Simulations

Inga C. Kuschnerus, Haotian Wen, Juanfang Ruan, Xinrui Zeng, Chun-Jen Su, U-Ser Jeng, George Opletal, Amanda S. Barnard, Ming Liu, Masahiro Nishikawa, and Shery L. Y. Chang*



Cite This: *ACS Nanosci. Au* 2023, 3, 211–221



Read Online

ACCESS |

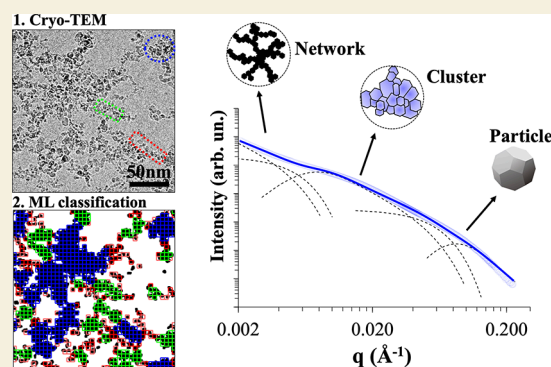
Metrics & More

Article Recommendations

Supporting Information

ABSTRACT: Understanding the polydispersity of nanoparticles is crucial for establishing the efficacy and safety of their role as drug delivery carriers in biomedical applications. Detonation nanodiamonds (DNDs), 3–5 nm diamond nanoparticles synthesized through detonation process, have attracted great interest for drug delivery due to their colloidal stability in water and their biocompatibility. More recent studies have challenged the consensus that DNDs are monodispersed after their fabrication, with their aggregate formation poorly understood. Here, we present a novel characterization method of combining machine learning with direct cryo-transmission electron microscopy imaging to characterize the unique colloidal behavior of DNDs. Together with small-angle X-ray scattering and mesoscale simulations we show and explain the clear differences in the aggregation behavior between positively and negatively charged DNDs. Our new method can be applied to other complex particle systems, which builds essential knowledge for the safe implementation of nanoparticles in drug delivery.

KEYWORDS: *detonation nanodiamonds, Cryo-TEM, SAXS, machine learning, coarse-grained molecular dynamics modeling*



INTRODUCTION

In last decades, various types of nanoparticles have been extensively studied for biomedical applications, given their immense potential for the improvement of drug delivery.^{1,2} The safety and efficacy of these nanocarriers are often limited by inadequate drug delivery to the target area or undesired side effects and severe toxicity. These concerns can be addressed with strictly controlled and predictable characteristics such as size and polydispersity.³ However, even monodisperse particles can face aggregation later during application due to the buffers and biological media, which may impact the nanoparticles' colloidal stability.^{4,5} Hence, reliable characterization of particle aggregation and assessment of their polydispersity are important to gain more understanding about their effect on the cell uptake and viability, release and molecular stability of the administered drug, and thereby help to improve the safety of new nanocarrier formulations.

Detonation nanodiamonds (DNDs), are 3–5 nm nanoparticles formed through a detonation process,⁶ which have recently sparked interest for the use in drug delivery,^{7–14} gene therapy,^{15–18} as biomarkers in bioimaging,^{19–21} tissue engineering, and bone surgery^{22–25} due to their excellent biocompatibility and flexibility in surface chemistry.

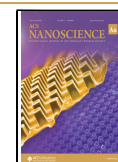
DNDs are commonly labeled as monodisperse in solution,^{26,27} which is usually confirmed by techniques such as dynamic light scattering (DLS) and small-angle X-ray scattering (SAXS). However, these characterization methods hold certain limitations. DLS only shows reliable size distributions for (quasi)-spherical particles, and the size distributions observable in SAXS are limited to approximately a couple of 100 nm (depending on the scattering length density) by the scattering angle. In the case of polydisperse and aggregated systems, SAXS can only give an indication about the shape and size distribution of the average aggregate morphology. As a result, SAXS and DLS are not suitable to obtain the distribution of individual aggregate morphologies. Such information is especially important in a biomedical context, since different particle shapes and aggregation may influence cell uptake and cell viability.²⁸ Moreover, newer research has revealed the polydisperse and aggregated nature of

Received: November 15, 2022

Revised: February 10, 2023

Accepted: February 10, 2023

Published: April 5, 2023



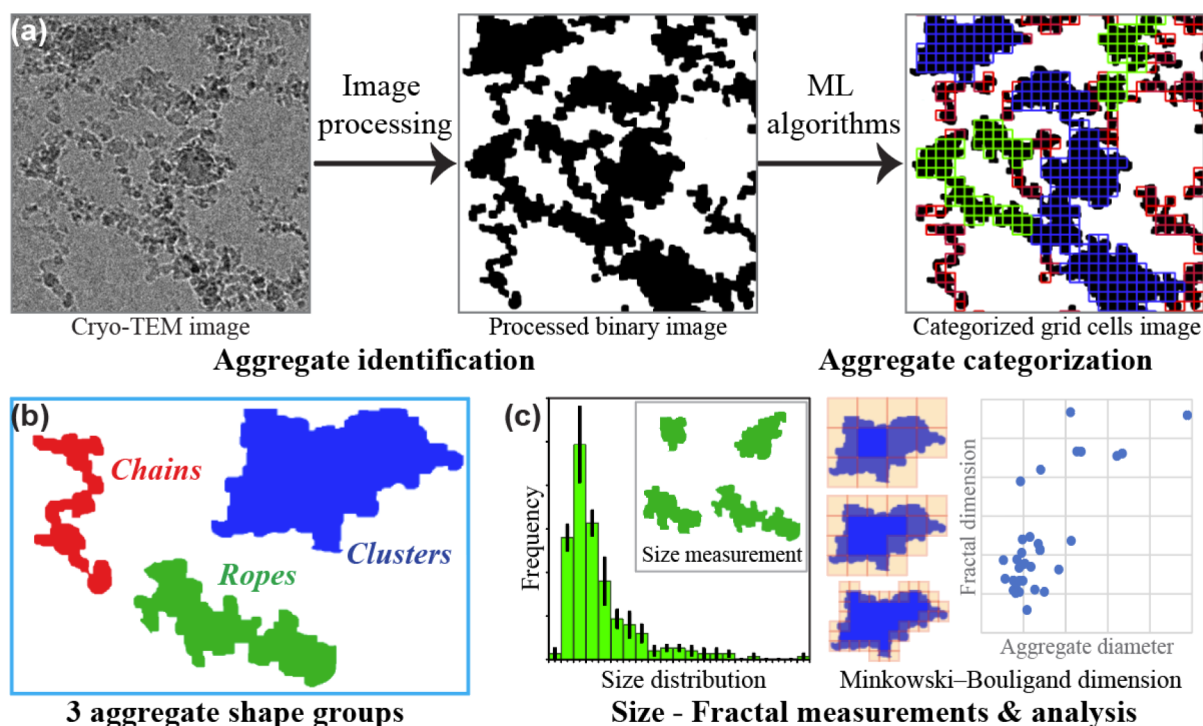


Figure 1. Scheme of the ML assisted cryo-TEM image analysis for (a) aggregate morphology identification and (b) categorization and (c) size and fractal dimension analysis.

DNDs in aqueous media,^{29–32} most likely due to their complex surface structures.^{5,33,34} Unlike standard colloidal systems where particle assembly and (prevention of) aggregation can be controlled by surfactants,^{27,35} theoretical calculations have shown that DNDs exhibit facet-dependent, unisotropic surface electrostatic potential distributions. These electrostatic potentials have been shown to promote ordered facet–facet connections resulting in chain and loop assemblies^{36,37} which have been observed using transmission electron microscopy (TEM) (see Figure S1).^{29,35} Considering the complex aggregation behavior and the limitations of DLS and SAXS, a more direct and unambiguous characterization method would be beneficial to improve the understanding of the colloidal properties of DNDs.

Here we present a machine learning (ML)-based cryo-TEM analysis of DND aggregates in aqueous media revealing the shape and size distributions of their different morphologies. Cryo-TEM, unlike conventional TEM, holds the advantages of imaging the sample frozen in its native state, hence providing information about the dynamic formation process at high spatial resolution. It has been previously used for DND suspension characterization;^{29,31,32} however, it has not been used to provide statistical analysis comparable with the bulk sample analysis like DLS and SAXS. Quantitative image analysis using ML allows us to process a large amount of image data and gain more statistics about the ensemble behavior of DNDs in solution. Combining ML and cryo-TEM as a characterization methodology provides additional information about the distribution of size and shape of individual aggregate components in a polydisperse nanoparticle system opposed to only averaged information in common scattering methods. Moreover, we present course-grained molecular dynamics approach-based mesoscale simulations of nanodiamond aggregation to provide insight into the formation mechanism of these complex aggregate morphologies. Based on our direct

imaging observation and statistical analysis of the experimental results, combined with the mesoscale simulations, we show that the DND suspensions in water exhibit strong and robust aggregates consisting of ropes and clusters. Such aggregate morphologies are intrinsic properties of the DND particles, where their surface electrostatic potential distributions are the dominating factor for the rope and cluster formation, and the reason why these ropes and clusters are stable against flocculation.

MATERIAL AND METHODS

Machine Learning for Aggregate Distribution from cryo-TEM Images

Our methodology is illustrated in the schematic diagram shown in Figure 1. The method is divided into three parts: the first part is the image preprocessing to separate the nanodiamond aggregates from the background. The second part is to apply the data sets to the ML algorithm for aggregate morphology labeling and categorized into shape groups. The final part is the evaluation of the categorized results and to obtain the relevant aggregate information including the size distributions and fractal dimension distributions.

In the first part, the background intensity in the raw image was removed by using the dynamic thresholding method³⁸ and then converted into binary image where the aggregates are initially identified. This method has been shown to be robust in removing often inhomogeneous background in the TEM images.³⁹ After the background removal, the aggregate identification still requires further improvement due to the nature that the cryo-TEM images are very noisy, as a low electron dose is required for imaging frozen samples. The aggregate identification improvement is carried out by using a combination of erosion and dilation,⁴⁰ and hole-filling⁴¹ methods, so that there are no “gap intensities” within the interior of the aggregates.

In the second part, unsupervised machine learning algorithm is used in order to label and categorize the aggregate morphologies without the use of the training data sets, and therefore the method is general in principle. This is done by first dividing the preprocessed

binary data into grid-cells (for example, see the green grid-cells illustrated in Figure 1a). The choice of the grid-cell is optimized to achieve high accuracy in shape categorization, by testing a range of grid-cell sizes from 3 to 16 nm. The optimum grid-cell size was determined to be 5 nm, which is approximately the size of the primary DND particle. Next, the grid-cell intensity histograms were initially categorized into three groups (k_n) to differentiate the image background (k_1), aggregate edges (k_2), and aggregate interiors (k_3), using the hierarchical agglomerative clustering method with the average linkage.⁴² Details regarding the machine learning clustering method can be found in refs 39 and 43. Then, a second categorization was further applied, to include the first and second order nearest neighbors of a given grid-cell, in order to differentiate aggregate morphologies. In this second categorization, we use the groups (k_n) obtained from the initial categorization as input, to further obtain three aggregate shape groups, s_n .

While our method can automatically categorize the shape groups, here we have predetermined the shape groups to be chain (s_1), rope (s_2), and cluster (s_3). Chains are defined to be one primary DND wide and ropes are less than three DND wide. Clusters are defined to have a diameter larger than the width of three primary DND. (More details of the shape labeling and categorization method can be found in the Supporting Information.) The choice of differentiating these three shapes groups has significance in the assembly formation mechanism (which is discussed in more detail in the Results and Discussion section). Moreover, it is based on our previous experimental observations that show particle size-dependent assembly behavior.^{29,44} The accuracy of the ML method has been verified through expert human manual counting of more than 10 representative images, giving <3% errors (in terms of the number of grid-cells).

In the third part, the resultant categorized aggregate shapes (Figure 1b) were analyzed to extract important aggregate parameters, namely the size distributions and their corresponding fractal dimensions (Figure 1c). This is done by first converting the categorized grid-cells in the shape groups (s_n) into the contour data sets. The areas enclosed by the aggregate contours were then calculated to estimate their sizes. In the case of the chain and rope aggregates their sizes refer to their lengths. The size of a cluster is approximated as the diameter of the disk. The fractal dimension is determined using the Minkowski–Bouligand method⁴⁵ from the contour of the cluster aggregates. This method calculates the fractal dimension, D , using the formula, $N(r) \approx C\left(\frac{1}{r}\right)^D$, where N is the total number of the “boxes” covering the cluster contour (illustrated as orange color boxes in Figure 1c), r is the dimension of the box, and C is a constant coefficient.

Course-Grained Molecular Dynamics Simulations of Nanodiamond Assembly. Simulation nanoparticle assembly using protoparticles (SNAP) was used to investigate the meso-structure of aggregated faceted polyhedral nanodiamonds. Details of the SNAP coarse-grained molecular dynamics approach have been published elsewhere.⁴⁶ The package has been used previously to investigate nanodiamond self-assembly,^{29,46,47} and we use the same polyhedral particle models and facet interactions here. Three particle shapes, the great rhombicuboctahedron (GRO), the small rhombicuboctahedron (SRO), and the modified truncated octahedron (mTO), were constructed with each polyhedra enclosed by low index {100}, {110}, and {111} facets, which were previously observed experimentally via TEM³⁵ (and additional examples can be found in Figure S1), and known to have characteristic positive, near-neutral and negative surface electrostatic potentials, respectively.³⁷ The facet–facet electrostatic potential was fit via density functional tight binding calculations of the orientation- and separation-dependent potential energy binding curves between pairs of atomistic nanodiamond models^{36,37} and is responsible for the aggregation and self-assembly. A polydispersed mixture at a density of 1.75×10^{18} particles/cm³ was simulated containing 20% GRO, 50% SRO and 30% mTO particles types, with each type having an experimentally motivated size (diameter) distribution of 20% at 2.2 nm, 50% at 2.7 nm and 30% at 3.2 nm (thus 9 distinct particles when including size). Postsimulation analysis focused on the time-dependent first, second,

and third nearest-neighbor coordination contributions from the different particle type/size pairs to investigate which sizes and types dominated the initial stages of aggregate assembly.

Detonation Nanodiamond Synthesis

Two different types of DND dispersions were chosen for comparison exhibiting different ζ -potentials. They are commercial DND dispersions obtained from Daicel Corporation (Osaka, Japan). The synthesis of the DNDs has been reported elsewhere.⁴⁸ In short, to produce the DND particles, 50:50 TNT:RDX charges were detonated in CO₂ atmosphere, and the detonation soot was purified in a mix of 70 wt % nitric acid and concentrated sulfuric acid in a 1:6 volume ratio at 150 °C for 5 h. The resulting powder was annealed in either hydrogen or in oxygen, at 350 °C in order to break down the intrinsic aggregates.

DNDs that have been annealed in hydrogen gives positive ζ -potential at 32.2 ± 1.8 mV, named DND-pos. here. Those annealed in oxygen gives negative ζ -potential at -40.3 ± 3.0 mV, named DND-neg. here.

Cryo-TEM. The DND samples were prepared via freeze-plunging method for cryo-TEM imaging. The process of rapid cooling transforms (within microseconds) water into vitreous ice, thereby preserving the native state of the DND aggregates in solution. Approximately 1 wt % of each sample in deionized water was sonicated for ca. 30 min prior to being prepared for cryo-TEM. Afterward, 4.5 μ L of sample was deposited as a droplet onto the glow-discharged grid (R2/2 Quantifoil copper grids, Jena, Germany) using a Leica grid plunger at 15 °C, 89% humidity, and a blotting time of 3.5 s. Images were acquired using a Talos Artica TEM (Thermo Fisher Scientific, Waltham, USA) with an acceleration voltage of 200 keV.

Small Angle X-ray Scattering. SAXS data were collected using the TPS 13A BioSAXS beamline of the Taiwan Photon Source (TPS) at the National Synchrotron Radiation Research Center (NSRRC), Hsinchu.⁴⁹ With a 10 keV beam and a sample-to-detector distance of 5.32 m, the SAXS data were collected at a sample temperature of 318 K using the Eiger X 9 M pixel detector in vacuum. The scattering vector $q = (4\pi)\sin(\theta)/\lambda$ is defined by the X-ray wavelength λ and scattering angle 2θ . More details can be found in the Supporting Information.

Here we analyze the DND aggregates using the Beaucage model which is better suited for hierarchical structures. It proposed a unified Guinier/power-law method which has proven to be a very appropriate tool to characterize multilevel structures. For an arbitrary number N of structural levels it can be written as⁵⁰

$$I = \sum_{i=1}^N [G_i \exp(-q^2 R_{g_i}^2/3) + B_i \exp(-q^2 R_{g_{i-1}}^2/3) \tilde{q}^{P_i}] \quad (1)$$

with $\tilde{q} = (\text{erf}(qR_{g_i}/6^{1/2}))^3/q$, $i = 1$ refers to the smallest structural level, i.e., $R_{g_1} = r_g$ and $R_{g_2} = R_g$ are the radius of gyration of the primary particles and the aggregates, respectively, P_i refers to the slopes with $p_1 = (6 - d_s)$ and $d_i = p_2$, and G_i is the Guinier prefactor of the i -th level structure. More information on the theory can be found in the Supporting Information.

Vibrational Spectroscopy. Approximately 10 μ L of each nanodiamond dispersion was placed on a clean diamond ATR crystal and allowed to air-dry in a desiccator for at least 1 h. Infrared spectroscopy was conducted using a Bruker Vertex80v FTIR spectrometer (Billerica, USA), equipped with a diamond ATR crystal. A background was taken prior to analysis of the dried dispersions, and the ATR crystal was cleaned with ethanol prior to each analysis. All analyses were conducted under vacuum, with 128 scans collected over the region of 4000–400 cm⁻¹.

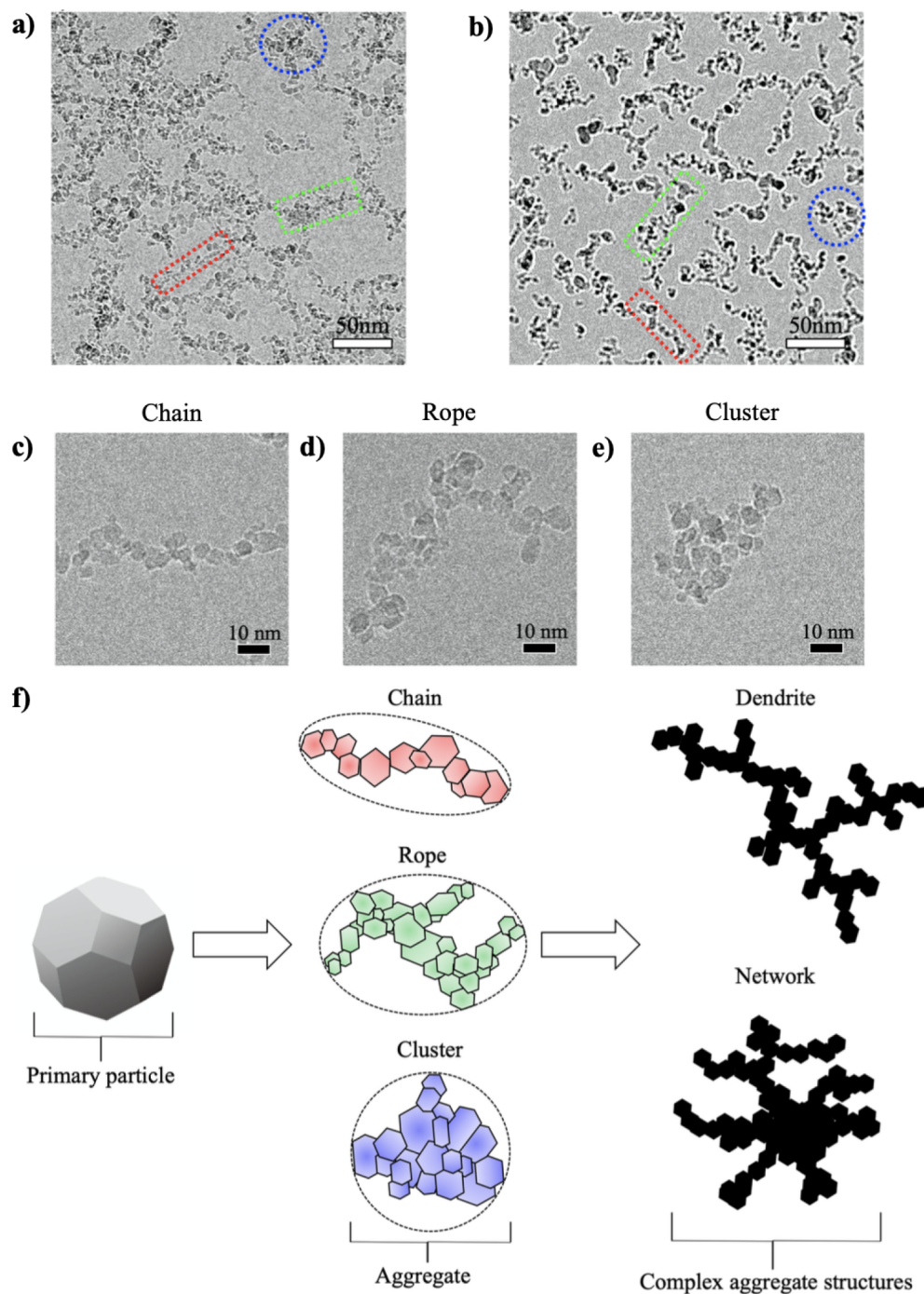


Figure 2. (a,b) Representative cryo-TEM images of DND samples DND-pos. and DND-neg., respectively. Cluster are indicated by blue circles, ropes by green and chains by red rectangles. (c–e) High-magnification cryo-TEM images of (c) chains, (d) ropes and (e) clusters. (f) Schematic diagram of hierarchical assembly behavior of DNDs in solution.

RESULTS AND DISCUSSION

Aggregate Morphology and Size Distributions

Figure 2 shows the cryo-TEM images of DND-pos. (Figure 2a) and DND-neg. (Figure 2b), respectively. The detonation synthesis process of these two samples is identical except that their the postsynthesis purification treatments (for removing non- sp^3 -bonded carbon) differ. The former is annealed in hydrogen where as the latter in oxygen. These two were chosen for comparisons as DND-pos. can bind negatively charged drugs or macromolecules such as DNA via

electrostatic interactions. DND-neg. on the other hand is often further functionalized or coated with positively charged polymers to reduce nonspecific adsorption of biomolecules and converting the charge to enable electrostatic binding of an anionic drug/biomolecule.⁵¹

Upon a first qualitative inspection of both samples via cryo-TEM images, the coexistence of three different aggregate morphologies: cluster, ropes and chains, becomes apparent. The chains refer to an ordered aggregate formed by connecting low index crystallographic facets of individual DND particles and have a nominal width of one particle (Figure 2c, and high-

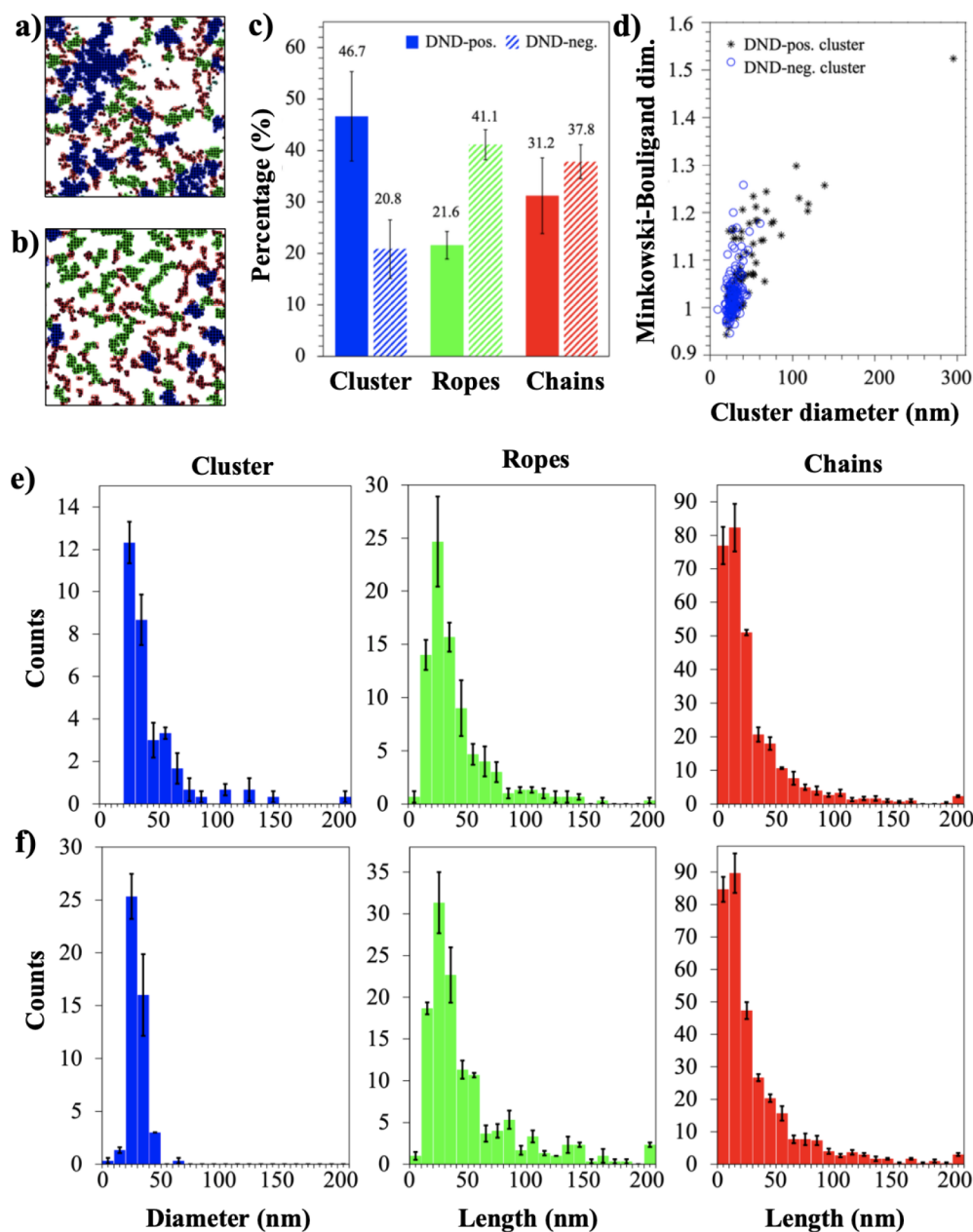


Figure 3. (a,b) ML categorized aggregate morphologies overlaid on the cryo-TEM images for DND-pos. and DND-neg., respectively. clusters are marked in blue, ropes in green and chains in red. (c) Ratio of each aggregate morphology for DND-pos. (solid bar) and DND-neg. (shaded bar). (d) Minkowski–Bouligand fractal dimension with respect to the cluster diameter of individual clusters for DND-pos. (black asterisk) and DND-neg. (blue circle). (e,f) Size distribution for clusters, ropes and chains for DND-pos. and DND-neg., respectively.

resolution TEM image showing connecting facets is given in Figure S1).

Ropes are like chains but wider in width with multiple branches (Figure 2d). The cluster morphology (Figure 2e) does not have any ordered interparticle connections. This observation is consistent with the previous reports.^{29,31,47} Moreover, there are clear visual differences between both samples: DND-neg. shows more chains and ropes which are forming dendrite-like structures, whereas DND-pos. exhibits more clusters that form larger networks. Figure 2f illustrates how the self-assembly of the presented DND samples in solution leads to hierarchical structures: As displayed in the schematic diagram, primary particles in the size range of ca. 5 nm form the three main aggregate morphologies which then

self-assemble into various types of complex aggregate structures.

Overall, such polydispersity and complex aggregate morphology distribution present in these DND dispersion can lead to inaccurate aggregate size measurement and interpretation if only conventional scattering techniques are used for measurements. To further quantify the aggregate size and morphology distribution as well as their fractal dimension, the ML assisted cryo-TEM imaging analysis that we developed here allows us to statistically assess the differences in the morphology distributions and additionally extract the diameter of clusters and length of chains and ropes (Figure 1).

In order to quantitatively compare images of the different samples without the influence of the concentration effects, it was ensured that the areal concentration of the DNDs (defined

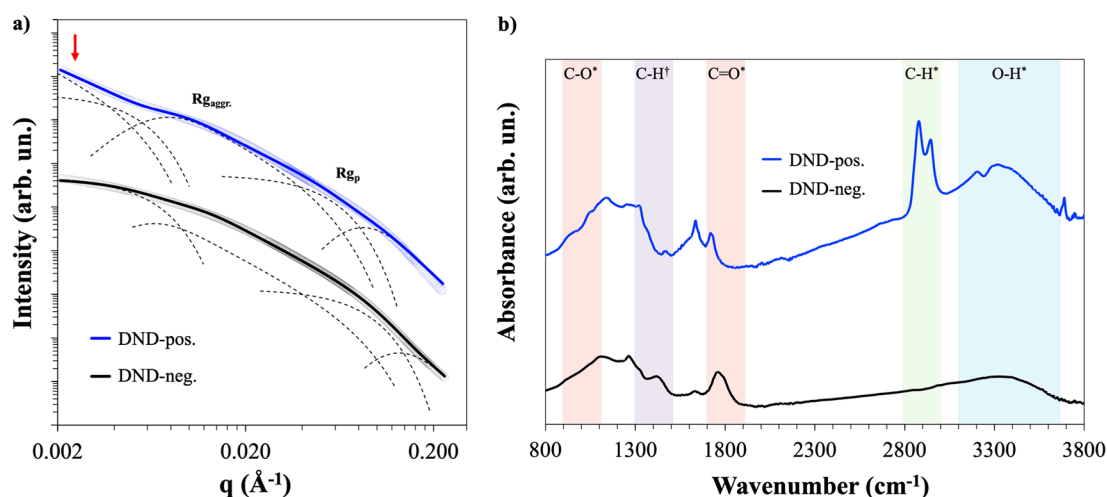


Figure 4. (a) Experimental and fitted SAXS intensity curves derived from a unified Beaucage model for DND-pos. (blue curve) and DND-neg. (black curve). The dashed lines illustrate the contributions of each structural level described in eq 1 to the full model. Red arrow points toward upturn in the spectra indicating network formation. (b) FTIR spectra for DND-pos. (blue curve) and DND-neg. (black curve). The spectra have been normalized and scaled for the sake of clarity. * indicates stretching vibrations; † bending vibrations.

as the projected areas of DND over the total areas of the image) are the same (approximately 35% for each sample). To ensure sufficient statistics multiple cryo-TEM showing ca. 20000 particles for each of the two samples were analyzed.

Figure 3a,b shows the results of the quantitative analysis using our ML method applied to cryo-TEM images. The ML categorized aggregate morphology distribution were overlaid onto the cryo-TEM images where clusters are marked in blue, ropes in green and chains in red (Figure 3a,b). The ratio of each aggregate morphology is quantitatively determined and shown in Figure 3c. It confirms that both samples exhibit a coexistence of chain, rope and cluster morphologies.

Moreover, it reveals differences in the chain, rope and cluster ratios for both samples. In sample DND-pos., the ratio of clusters is almost doubled (46.7%) in comparison to DND-neg. (20.8%). In contrast, DND-neg. has almost twice as many ropes (41.1%). The ratio for chains is similar for DND-pos. and DND-neg. with 31.2% and 37.8%, respectively.

Figure 3e,f shows the extracted size information for cluster, ropes and chains in both samples. Each error bar represents the standard deviation of the aggregate distribution across the multiple images analyzed.

Despite DND-neg. showing more rope and chain morphologies, the size distribution of ropes and chains for both samples is similar to their lengths ranging from 10 to 200 nm peaking at 25 nm for ropes and at 15 nm for chains in both samples. However, the cluster diameter for sample DND-neg. has a narrower distribution ranging mostly from 20 to 50 nm peaking at ca. 25 nm, whereas DND-pos. has a wider distribution ranging up to 200 nm.

Additionally, our method is able to extract and analyze the fractal dimension of individual clusters, therefore giving the fractal dimension distributions rather than the averaged dimension as in SAXS. Figure 3d shows the scatter plot of the cluster diameter vs the Minkowski-Bouligand dimension showing a narrower distribution for DND-neg. with a fractal dimension between 0.95 and 1.1 representing dendritic structures, whereas the fractal dimension of DND-pos. is more scattered, ranging from 1 to 1.2 with small fractions of larger clusters around 1.3. This is closer represented by “dragon curve” structures,⁵² exhibiting more interconnected,

tighter structures. Overall, our quantitative analysis accurately reveals the detailed difference in the colloidal behavior of both samples, which is manifested in the higher ratio of cluster aggregates, less ropes and chains, and more interconnected aggregate structures for DND-pos. compared to DND-neg.

Comparison with SAXS Analysis

Having established our ML-based cryo-TEM imaging analysis method for measuring the polydisperse aggregate morphology, size distributions as well as the fractal dimension, we have also conducted comparative SAXS measurement. Figure 4a shows the experimental and fitted SAXS intensity curves for DND-pos. (blue curve) and DND-neg. (black curve). Regardless of their ζ -potential, both curves show at least two different size populations (aggregates and primary particles), indicated by the two transitions in the scattering curve ($R_{g,agg}$ and $R_{g,p}$, respectively). Importantly, only DND-pos. shows an upturn at a low q -range indicating the presence of a third population that is larger than $R_{g,agg}$. This is in good agreement with our cryo-TEM image analysis.

Table 1 summarizes the different radii for primary particles and aggregates derived from fitting the experimental SAXS data using the Beaucage model, as well as the dimension variable S and Porod constant FD_m extracted from a Guinier–Porod fit.

Table 1. DND Average Size and Morphology Analysis Derived from SAXS and ML/cryo-TEM Analysis^{abcd}

Sample	$R_{g,agg}$ (nm)	$R_{g,p}$ (nm)	FD	S	R_m (nm)	FD_m
DND-pos.	38.4	3.6	2.30	1.42	43.6 ± 34.7	1.08 ± 0.09
DND-neg.	30.9	2.3	2.22	0.98	28.7 ± 6.8	1.03 ± 0.05

^a $R_{g,agg}$ refers to the radii of the aggregates and $R_{g,p}$ to the radii of the primary particles analyzed using Beaucage model; FD refers to the fractal dimension (Porod constant) of the aggregates and S to the dimension variable, analyzed using Guinier–Porod model. FD_m refers to Minkowski–Bouligand fractal dimensions and R_m refers to the averaged aggregate size derived from the ML-based cryo-TEM image analysis method. ^b $S = 0$: spheres. ^c $S = 1$: rods. ^d $S = 2$: platelets.

The Beaucage model has been demonstrated to be well suited for measuring particle and aggregate sizes in complex hierarchical structures,^{53–55} and the more simplified Guinier–Porod model was additionally applied to the SAXS data (Figure S2) to gather more information about the morphology of the aggregates. To quantitatively compare the SAXS measurement with our ML assisted image analysis, we also included the averaged value of the aggregate size (with the standard deviation indicating the spread of the size distributions) and the fractal dimension determined using the Minkowski–Bouligand method. It should be noted here that the Minkowski–Bouligand fractal dimension is not the same as the Porod exponent but can be compared relatively. Based on the SAXS measurements, the primary particle radii for DND-pos. and DND-neg. are 3.6 and 2.3 nm and the aggregate radii are 38.4 and 30.9 nm, respectively.

The extracted dimension variable S of 1.42 presented in Table 1 suggests a more plate-like morphology for DND-pos. On the other hand, DND-neg. has a S value of 0.98 which is closer to a rod-like morphology. The fractal dimensions (Porod exponent) of DND-pos. and DND-neg. are 2.3 and 2.2, respectively. The Porod exponent values of less <3 suggest both DNDs exhibit fractal structures, with DND-pos. giving slightly more dense structures.

These SAXS analysis results are in excellent agreement with our quantitative analysis using the ML assisted method. First, the higher combined fraction of 79% of chains and ropes in the DND-neg. sample compared to 53% in the DND-pos. sample is nicely reflected by the lower dimension variable S of rod-like structures in the SAXS measurement of the former sample. Second, the size averaged through all aggregates based on our method quantitatively agrees well with the SAXS aggregate size measurement. DND-pos. appears to be a higher average size compared to SAXS measurement. One explanation could be the large deviation in the aggregate size distribution present in DND-pos., leading to a biased average toward a higher value. Based on these comparisons, it is important to highlight that while SAXS is excellent for bulk analysis, e.g., averaged aggregation behavior, the image-based combined ML-based cryo-TEM analysis method can provide additional complementary and statistical information regarding the individual aggregate behavior. This information can be critical in understanding more complex and polydisperse systems. Overall, combining ML and cryo-TEM holds the advantage of giving a more detailed distinction of both samples.

Surface Chemistry

DND particle surfaces are known to contain multiple coexisting functional groups including ketones, aldehydes, amines, hydroxyl, and hydrogen, which are leftover from the purification process.¹⁰ FTIR measurements were conducted here to confirm the differences in surface chemistry of the samples. Figure 4b shows the FTIR spectra for both DND-pos. (blue line) and DND-neg. (black line). The spectra of the samples DND-neg. is rich in carboxylic groups with a prominent peak at 1720–1740 cm^{-1} . DND-pos. shows distinct C–H stretching vibration and O–H stretching at approximately 2867–2981 cm^{-1} and 3200–3550 cm^{-1} . Despite the differences in their surface chemistry, they both show the coexistence of three aggregate morphologies, although with different ratios and size distributions. Therefore, the surface chemistry is likely to play a role in moderating the ratios of the aggregate morphologies.

Aggregate Assembly Formation Mechanism and Dynamics

To elucidate why the equilibrium aggregate structures of chain, rope, and cluster morphologies are present in the DND samples and their formation kinetics, mesoscale calculations using the course-grained molecular dynamics approach (using SNAP code⁴⁶) were conducted using 25000 particles with varying particle sizes and shapes. The particle shapes considered here are the great rhombicuboctahedron (GRO), the small rhombicuboctahedron (SRO), and the modified truncated octahedron (mTO) constructed with each polyhedra enclosed by low index $\{100\}$, $\{110\}$, and $\{111\}$ facets. The choice of including these three facet types is based on the experimental observation via TEM,³⁵ which never showed the presence of any other higher index facets, and are known to have characteristic positive, near-neutral, and negative surface electrostatic potentials, respectively.^{46,47,56} The sizes chosen are 2.2, 2.7, and 3.2 nm for each particle shape (details of the simulation method and parameters can be found in the Supporting Information). Effects of size and shape polydispersity have been investigated previously showing a size and shape dependent assembly process.^{44,47} Hence, this work uses combinations of three particle sizes and three different particle shapes resulting in 45 unique particle pair type combinations. Figure 5a displays the assembly of 25000 particles.

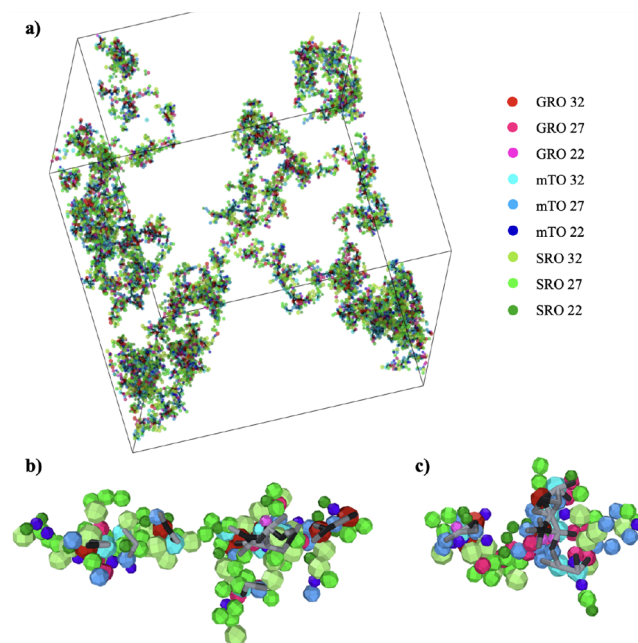


Figure 5. (a) SNAP modeling for clusters in larger volume. (b,c) Cluster extractions from SNAP modeling with the corresponding bond diagram (in gray color) showing the connections between the fastest ordering particles.

Distributions of aggregates with chains and ropes branches and clusters are present which is qualitatively in agreement with our experimental observations. Exemplar rope and cluster aggregate structures are shown in Figure 5b,c.

To gain more understanding about the kinetics of the aggregate formation, the coordination contribution was calculated for all particle type/size combinations as a function of time looking at the first, second and third nearest neighbors. An example for the first nearest neighbor contributions is

Table 2. Fastest and Slowest Pair to Assemble According to SNAP Model^a

No.	First nearest neighbor	Second nearest neighbor	Third nearest neighbor
Fastest pair to assemble			
1	mTO 32 - mTO 32	mTO 32 - mTO 32	mTO 32 - mTO 32
2	mTO 32 - GRO 27	mTO 32 - mTO 27	mTO 27 - mTO 27
3	mTO 32 - mTO 27	mTO 27 - GRO 32	mTO 32 - mTO 27
4	mTO 32 - GRO 32	mTO 32 - GRO 32	mTO 27 - GRO 27
5	mTO 27 - GRO 32	mTO 27 - mTO 27	mTO 32 - GRO 27
Slowest pair to assemble			
1	SRO 22 - SRO 22	SRO 22 - SRO 22	SRO 22 - SRO 22
2	GRO 22 - GRO 22	SRO 22 - mTO 22	mTO 22 - GRO 22
3	SRO 22 - GRO 22	mTO 22 - GRO 22	SRO 22 - GRO 22
4	mTO 22 - GRO 22	SRO 22 - GRO 22	SRO 22 - mTO 22
5	SRO 22 - mTO 22	SRO 22 - SRO 32	mTO 22 - mTO 22

^amTO: modified truncated octahedron; GRO: great rhombicuboctahedron, SRO: small rhombicuboctahedron; and 22, 27, and 32 refer to the overall size of the particles in Å.

found in the Supporting Information in Figure S4. The fastest and slowest pairs that begin increasing their coordination (to start assembly) are outlined in Table 2 (and correspond to the blue and red lines in Figure S4).

Initiation of assembly, as the simulation temperature is decreased, is shape and size dependent with preference for larger mTO (dominated by negatively charged {111} surface area) and GRO (dominated by positively charged {100} surface area) particles shapes. This effect is even more pronounced considering that SRO (dominated by neutral {110} surface area) particles make up 50% of all particles in the simulation. The different particle shapes are shown in Figure S3. The picture that emerges is that the first particle pairs to connect are the largest 3.2 nm mTO pairs dominated by a negative surface area, which after a delay are also the first to appear in the second shell and subsequently the third shell. These findings are consistent with previous SNAP simulations at higher density which also showed that larger particles dominated early assembly forming chains as measured by the Lindemann index.^{44,47} The smallest and near-neutral SRO particles end up lining the pore surfaces of the aggregates (assembling last). With these findings, the final, quenched simulation configuration was decomposed into chain, rope, and cluster formation. The surface chemistry of DNDs plays a minor role, individual isolated structures where the member particles of a common structure have some nearest neighbor path connecting them. Some examples of these are shown in Figure 5 including the largest structure found Figure 5a. Additionally, the five fastest type/size pairs from Table 2 which are neighbors are highlighted in Figure 5b,c via black line connections. As expected, larger mTO and GRO particles tend to form central backbones of many of these structures in line with their dominance in Table 2. Then a mixture of mTO, GRO, and SRO particles attach to the backbones to form ropes. The neutral SRO particles attach last to form ropes and clusters. While these SNAP simulations are performed in vacuum and neglect the surface functional group interactions with water, the excellent agreement between the experimental analysis and the simulations strongly indicates that the formation mechanism of the three aggregate morphologies is largely based on the distribution of surface electrostatic potentials. The picture that emerges is that the large, faceted particles tend to assemble first, forming a structural backbone of chains. The weaker interacting particles with a near-neutral surface area and small sizes assemble last on the outside of

these structures to form ropes and clusters. This potentially makes two such structures neutral to each other and stops their coalescence. With the results of the mesoscale calculation, it is then evident that the ratio of primary particle sizes and shapes is the dominating factor in terms of self-assembly and aggregation morphology.

CONCLUSIONS

In conclusion, we have demonstrated a newly developed particle aggregate characterization method by combining cryo-TEM imaging with unsupervised ML for measuring the particle aggregate dispersion in their native state. This new method allows us to analyze the complex aggregate system of DNDs unambiguously, quantitatively and statistically, giving critical information on aggregate morphology and size distribution as well as their fractal dimension. The results show that purified DND dispersions in water exhibit coexistence of chains, ropes, and cluster structures of varying ratios, regardless of their ζ -potential. However, size distribution analysis of the different morphologies shows that the cluster size distribution for DND-pos. is broader with significant fractions of larger sized clusters, while DND-neg. has a narrower and smaller cluster size distribution. Moreover, DND-pos. shows a higher fractal dimension, indicating a network formation, which is not present in the DND-neg. sample. This is consistent with the SAXS measurements, yet our ML-based cryo-TEM image analysis method still offers more information by quantitatively showing the differences in size distribution and fractal dimension. The mechanism of the coexistence of the three morphologies is dominated by the anisotropic electrostatic potential distributions of the nanodiamond particles. The larger primary particles with dominating positively or negatively charged surface electrostatic potential form the chain morphology first and become the backbones of ropes and cluster assembly, which are formed by attaching the smaller and near-neutral particles to the backbones. The dispersion stabilizes eventually due the near-neutral particles coating the surface aggregates, preventing further aggregation and flocculation, which explains the long-term colloidal stability of DND-aggregates. Moreover, the SNAP simulation reveals that it is the ratio of the sizes and shapes of primary particle that has the biggest influence on the aggregation morphology distribution. The surface chemistry, on the other hand, can moderate the ratio of the aggregate morphologies. For example, it has been shown theoretically that the presence

of the C–H group on the surface can weaken the nanodiamond interparticle interaction and disrupt the assembly ordering, thereby promoting the formation of random cluster aggregates.³⁶ This explains that the DND-pos. which is rich in C–H groups has higher ratios of clusters compared to DND-neg. Overall our results presented here offer potential solutions for controlling aggregate morphologies for specific biomedical applications. Fabricating larger particles with less C–H groups can promote the formation of chains and ropes, which offer higher surface areas for drug biomolecule absorption, and the elongated aggregate shapes can be beneficial for cellular uptake through penetration of the membranes. On the other hand, the smaller DND particles rich in C–H surface groups promote clusters which can be utilized as nanoporous structures. The robustness of the aggregate formation provides possibilities and flexibility of controlling aggregate morphologies and distributions tailored toward the needs of the desired applications.

■ ASSOCIATED CONTENT

SI Supporting Information

The Supporting Information is available free of charge at <https://pubs.acs.org/doi/10.1021/acsnanoscienceau.2c00055>.

Additional information regarding the detonation nanodiamond synthesis, high-resolution TEM of DND, labeling and categorization of aggregate morphology via unsupervised machine learning, SAXS analysis and details of the SNAP simulation (PDF)

■ AUTHOR INFORMATION

Corresponding Author

Shery L. Y. Chang – School of Materials Science and Engineering, University of New South Wales, Sydney, New South Wales 2052, Australia; Electron Microscope Unit, Mark Wainwright Analytical Centre, University of New South Wales, Sydney, New South Wales 2052, Australia; orcid.org/0000-0001-7514-4584; Email: shery.chang@unsw.edu.au

Authors

Inga C. Kuschnerus – School of Materials Science and Engineering, University of New South Wales, Sydney, New South Wales 2052, Australia; Electron Microscope Unit, Mark Wainwright Analytical Centre, University of New South Wales, Sydney, New South Wales 2052, Australia
Haotian Wen – School of Materials Science and Engineering, University of New South Wales, Sydney, New South Wales 2052, Australia
Juanfang Ruan – Electron Microscope Unit, Mark Wainwright Analytical Centre, University of New South Wales, Sydney, New South Wales 2052, Australia
Xinrui Zeng – School of Materials Science and Engineering, University of New South Wales, Sydney, New South Wales 2052, Australia
Chun-Jen Su – National Synchrotron Radiation Research Center, Hsinchu 30076, Taiwan
U-Ser Jeng – National Synchrotron Radiation Research Center, Hsinchu 30076, Taiwan; Department of Chemical Engineering, National Tsing Hua University, Hsinchu 30013, Taiwan; orcid.org/0000-0002-2247-5061
George Opletal – CSIRO Data61, Clayton, Victoria 3168, Australia

Amanda S. Barnard – School of Computing, Australian National University, Acton, Australian Capital Territory 2601, Australia; orcid.org/0000-0002-4784-2382

Ming Liu – Daicel Corporation, Osaka 530-0011, Japan

Masahiro Nishikawa – Daicel Corporation, Osaka 530-0011, Japan

Complete contact information is available at:

<https://pubs.acs.org/10.1021/acsnanoscienceau.2c00055>

Author Contributions

I.C.K. and H.W. contributed equally to this work. S.L.Y.C. conceived and supervised the study. I.C.K. and J.R. conducted the cryo-TEM experiments. H.W. developed the ML code and conducted the aggregate analysis. S.L.Y.C. conducted HRTEM and FTIR experiments. C.-J.S. and U.-S.J. conducted SAXS experiments and analysis. G.O. and A.S.B. conducted SNAP simulations. M.L. and M.N. conducted synthesis of DND particles. I.C.K. and S.L.Y.C. wrote the manuscript, and all other authors contributed to the writing. CRediT: **Xinrui Zeng** formal analysis (supporting).

Notes

The authors declare no competing financial interest.

■ ACKNOWLEDGMENTS

S.L.Y.C. and I.C.K. acknowledge the use of TEMs at the Electron Microscope Unit, Mark Wainwright Analytical Centre, UNSW. S.L.Y.C. acknowledges the use of vibrational spectroscopy facility at the University of Sydney. The authors acknowledge the SAXS data collection at NSRRC during the COVID-19 pandemic. S.L.Y.C. acknowledges the support by the Australian Research Council (ARC) under grant IC210100056.

■ REFERENCES

- (1) McNamara, K.; Tofail, S. A. M. Nanoparticles in biomedical applications. *Advances in Physics: X* **2017**, *2*, 54–88.
- (2) Suri, S. S.; Fenniri, H.; Singh, B. Nanotechnology-based drug delivery systems. *Journal of Occupational Medicine and Toxicology* **2007**, *2*, 16.
- (3) Danaei, M.; Dehghankhold, M.; Ataei, S.; Hasanzadeh Davarani, F.; Javanmard, R.; Dokhani, A.; Khorasani, S.; Mozafari, M. R. Impact of Particle Size and Polydispersity Index on the Clinical Applications of Lipidic Nanocarrier Systems. *Pharmaceutics* **2018**, *10*, 57.
- (4) Moore, T. L.; Rodriguez-Lorenzo, L.; Hirsch, V.; Balog, S.; Urban, D.; Jud, C.; Rothen-Rutishauser, B.; Lattuada, M.; Petri-Fink, A. Nanoparticle colloidal stability in cell culture media and impact on cellular interactions. *Chem. Soc. Rev.* **2015**, *44*, 6287–6305.
- (5) Bradac, C.; Rastogi, I. D.; Cordina, N. M.; Garcia-Bennett, A.; Brown, L. J. Influence of surface composition on the colloidal stability of ultra-small detonation nanodiamonds in biological media. *Diamond Relat. Mater.* **2018**, *83*, 38–45.
- (6) Krüger, A.; Kataoka, F.; Ozawa, M.; Fujino, T.; Suzuki, Y.; Aleksenskii, A. E.; Vul', A. Y.; Ōsawa, E. Unusually tight aggregation in detonation nanodiamond: Identification and disintegration. *Carbon* **2005**, *43*, 1722–1730.
- (7) Ho, D.; Wang, C.-H. K.; Chow, E. K.-H. Nanodiamonds: The intersection of nanotechnology, drug development, and personalized medicine. *Science Advances* **2015**, *1*, e1500439.
- (8) Chauhan, S.; Jain, N.; Nagaich, U. Nanodiamonds with powerful ability for drug delivery and biomedical applications: Recent updates on in vivo study and patents. *Journal of Pharmaceutical Analysis* **2020**, *10*, 1–12.

- (9) Perevedentseva, E.; Lin, Y.-C.; Cheng, C.-L. A review of recent advances in nanodiamond-mediated drug delivery in cancer. *Expert Opinion on Drug Delivery* **2021**, *18*, 369–382.
- (10) Mochalin, V. N.; Pentecost, A.; Li, X.-M.; Neitzel, I.; Nelson, M.; Wei, C.; He, T.; Guo, F.; Gogotsi, Y. Adsorption of Drugs on Nanodiamond: Toward Development of a Drug Delivery Platform. *Mol. Pharmaceutics* **2013**, *10*, 3728–3735.
- (11) Giammarco, J.; Mochalin, V. N.; Haeckel, J.; Gogotsi, Y. The adsorption of tetracycline and vancomycin onto nanodiamond with controlled release. *J. Colloid Interface Sci.* **2016**, *468*, 253–261.
- (12) Beltz, J.; Pfaff, A.; Abdullahi, I. M.; Cristea, A.; Mochalin, V. N.; Ercal, N. Effect of nanodiamond surface chemistry on adsorption and release of tiopronin. *Diamond Relat. Mater.* **2019**, *100*, 107590.
- (13) Turcheniuk, K.; Mochalin, V. N. Biomedical applications of nanodiamond. *Nanotechnology* **2017**, *28*, 252001.
- (14) Benson, V.; Amini, A. Why nanodiamond carriers manage to overcome drug resistance in cancer. *Cancer Drug Resist* **2020**, *3*, 854–866.
- (15) Bertrand, J.-R.; Pioche-Durieu, C.; Ayala, J.; Petit, T.; Girard, H. A.; Malvy, C. P.; Le Cam, E.; Treussart, F.; Arnault, J.-C. Plasma hydrogenated cationic detonation nanodiamonds efficiently deliver to human cells in culture functional siRNA targeting the Ewing sarcoma junction oncogene. *Biomaterials* **2015**, *45*, 93–98.
- (16) Leung, H. M.; Chan, M. S.; Liu, L. S.; Wong, S. W.; Lo, T. W.; Lau, C.-H.; Tin, C.; Lo, P. K. Dual-Function, Cationic, Peptide-Coated Nanodiamond Systems: Facilitating Nuclear-Targeting Delivery for Enhanced Gene Therapy Applications. *ACS Sustainable Chem. Eng.* **2018**, *6*, 9671–9681.
- (17) Zhang, X.-Q.; Chen, M.; Lam, R.; Xu, X.; Ōsawa, E.; Ho, D. Polymer-Functionalized Nanodiamond Platforms as Vehicles for Gene Delivery. *ACS Nano* **2009**, *3*, 2609–2616.
- (18) Chen, M.; Zhang, X.-Q.; Man, H. B.; Lam, R.; Chow, E. K.; Ho, D. Nanodiamond Vectors Functionalized with Polyethylenimine for siRNA Delivery. *J. Phys. Chem. Lett.* **2010**, *1*, 3167–3171.
- (19) Hong, G.; Diao, S.; Antaris, A. L.; Dai, H. Carbon Nanomaterials for Biological Imaging and Nanomedicinal Therapy. *Chem. Rev.* **2015**, *115*, 10816–10906.
- (20) Kuo, Y.; Hsu, T.-Y.; Wu, Y.-C.; Chang, H.-C. Fluorescent nanodiamond as a probe for the intercellular transport of proteins in vivo. *Biomaterials* **2013**, *34*, 8352–8360.
- (21) Hou, W.; Toh, T. B.; Abdullah, L. N.; Yvonne, T. W. Z.; Lee, K. J.; Guenther, I.; Chow, E. K.-H. Nanodiamond–Manganese dual mode MRI contrast agents for enhanced liver tumor detection. *Nanomedicine: Nanotechnology, Biology and Medicine* **2017**, *13*, 783–793.
- (22) Fox, K.; Ratwatte, R.; Booth, M. A.; Tran, H. M.; Tran, P. A. High Nanodiamond Content-PCL Composite for Tissue Engineering Scaffolds. *Nanomaterials* **2020**, *10*, 948.
- (23) Nunes-Pereira, J.; Silva, A.; Ribeiro, C.; Carabineiro, S.; Buijnsters, J.; Lanceros-Méndez, S. Nanodiamonds/poly(vinylidene fluoride) composites for tissue engineering applications. *Composites Part B: Engineering* **2017**, *111*, 37–44.
- (24) Zhang, Q.; Mochalin, V. N.; Neitzel, I.; Knoke, I. Y.; Han, J.; Klug, C. A.; Zhou, J. G.; Lelkes, P. I.; Gogotsi, Y. Fluorescent PLLA-nanodiamond composites for bone tissue engineering. *Biomaterials* **2011**, *32*, 87–94.
- (25) Zhang, Q.; Mochalin, V. N.; Neitzel, I.; Hazeli, K.; Niu, J.; Kontsos, A.; Zhou, J. G.; Lelkes, P. I.; Gogotsi, Y. Mechanical properties and biomineralization of multifunctional nanodiamond-PLLA composites for bone tissue engineering. *Biomaterials* **2012**, *33*, 5067–5075.
- (26) Terada, D.; Segawa, T. F.; Shames, A. I.; Onoda, S.; Ohshima, T.; Ōsawa, E.; Igarashi, R.; Shirakawa, M. Monodisperse Five-Nanometer-Sized Detonation Nanodiamonds Enriched in Nitrogen-Vacancy Centers. *ACS Nano* **2019**, *13*, 6461–6468.
- (27) Ōsawa, E. Monodisperse single nanodiamond particulates. *Pure Appl. Chem.* **2008**, *80*, 1365–1379.
- (28) Boselli, L.; Lopez, H.; Zhang, W.; Cai, Q.; Giannone, V. A.; Li, J.; Moura, A.; de Araujo, J. M.; Cookman, J.; Castagnola, V.; Yan, Y.; Dawson, K. A. Classification and biological identity of complex nano shapes. *Communications Materials* **2020**, *1*, 35.
- (29) Chang, S. L. Y.; Reineck, P.; Williams, D.; Bryant, G.; Opletal, G.; El-Demrashed, S. A.; Chiu, P.-L.; Ōsawa, E.; Barnard, A. S.; Dwyer, C. Dynamic self-assembly of detonation nanodiamond in water. *Nanoscale* **2020**, *12*, 5363–5367.
- (30) Tomchuk, O. V.; Avdeev, M. V.; Aleksenskii, A. E.; Vul, A. Y.; Ivankov, O. I.; Ryukhtin, V. V.; Füzi, J.; Garamus, V. M.; Bulavin, L. A. Sol–Gel Transition in Nanodiamond Aqueous Dispersions by Small-Angle Scattering. *J. Phys. Chem. C* **2019**, *123*, 18028–18036.
- (31) Kuznetsov, N. M.; Belousov, S. I.; Bakirov, A. V.; Chvalun, S. N.; Kamyshevsky, R. A.; Mikhutkin, A. A.; Vasiliev, A. L.; Tolstoy, P. M.; Mazur, A. S.; Eidelman, E. D.; Yudina, E. B.; Vul, A. Y. Unique rheological behavior of detonation nanodiamond hydrosols: The nature of sol-gel transition. *Carbon* **2020**, *161*, 486–494.
- (32) Knizhnik, A. A.; Polynskaya, Y. G.; Sinitits, A. S.; Kuznetsov, N. M.; Belousov, S. I.; Chvalun, S. N.; Potapkin, B. V. Analysis of structural organization and interaction mechanisms of detonation nanodiamond particles in hydrosols. *Phys. Chem. Chem. Phys.* **2021**, *23*, 674–682.
- (33) Pina-Salazar, E.-Z.; Urita, K.; Hayashi, T.; Futamura, R.; Vallejos-Burgos, F.; Wloch, J.; Kowalczyk, P.; Wisniewski, M.; Sakai, T.; Moriguchi, I.; Terzyk, A. P.; Ōsawa, E.; Kaneko, K. Water Adsorption Property of Hierarchically Nanoporous Detonation Nanodiamonds. *Langmuir* **2017**, *33*, 11180.
- (34) Chang, S. L. Y.; Dwyer, C.; Ōsawa, E.; Barnard, A. S. Size dependent surface reconstruction in detonation nanodiamonds. *Nanoscale Horizons* **2018**, *3*, 213–217.
- (35) Chang, S. L. Y.; Ōsawa, E.; Barnard, A. S. Confirmation of the electrostatic self-assembly of nanodiamonds. *Nanoscale* **2011**, *3*, 958–962.
- (36) Lai, L.; Barnard, A. S. Interparticle Interactions and Self-Assembly of Functionalized Nanodiamonds. *J. Phys. Chem. Lett.* **2012**, *3*, 896–901.
- (37) Barnard, A. S. Self-assembly in nanodiamond agglutinates. *J. Mater. Chem.* **2008**, *18*, 4038–4041.
- (38) Davies, E. R. *Machine vision: theory, algorithms, practicalities*; Elsevier, 2004.
- (39) Wen, H.; Luna-Romera, J. M.; Riquelme, J. C.; Dwyer, C.; Chang, S. L. Y. Statistically Representative Metrology of Nanoparticles via Unsupervised Machine Learning of TEM Images. *Nanomaterials* **2021**, *11*, 2706.
- (40) Liang, Z.; Nie, Z.; An, A.; Gong, J.; Wang, X. A particle shape extraction and evaluation method using a deep convolutional neural network and digital image processing. *Powder Technol.* **2019**, *353*, 156–170.
- (41) Li, G.; Zhang, Y.; Xu, B.; Li, X. Image Analysis and Processing of Skin Cell Injury Based on OpenCV. *Journal of Physics: Conference Series* **2019**, *1237*, 032003.
- (42) Jain, A. K. Data clustering: 50 years beyond K-means. *Pattern Recognition Letters* **2010**, *31*, 651–666.
- (43) Bishop, C. M.; Nasrabadi, N. M. *Pattern recognition and machine learning*; Springer, 2006; Vol. 4.
- (44) Opletal, G.; Barnard, A. S. Simulating Facet-Dependent Aggregation and Assembly of Mixtures of Polyhedral Nanoparticles. *Advanced Theory and Simulations* **2022**, *5*, 2100279.
- (45) Napolitano, A.; Ungania, S.; Cannata, V. Fractal dimension estimation methods for biomedical images. *MATLAB—A fundamental tool for scientific computing and engineering applications*; InTech, 2012; Vol. 3 pp 161–178.
- (46) Opletal, G.; Golebiewski, M.; Barnard, A. S. Simulated nanoparticle assembly using protoparticles (SNAP). *Journal of Physics: Materials* **2020**, *3*, 026001.
- (47) Opletal, G.; Chang, S. L.; Barnard, A. S. Simulating facet-dependent aggregation and assembly of distributions of polyhedral nanoparticles. *Nanoscale* **2020**, *12*, 19870–19879.
- (48) Yoshikawa, T.; Liu, M.; Chang, S. L. Y.; Kuschnerus, I. C.; Makino, Y.; Tsurui, A.; Mahiko, T.; Nishikawa, M. Steric Interaction

of Polyglycerol-Functionalized Detonation Nanodiamonds. *Langmuir* **2022**, *38*, 661–669.

(49) Shih, O.; et al. Performance of the new biological small- and wide-angle X-ray scattering beamline 13A at the Taiwan Photon Source. *J. Appl. Crystallogr.* **2022**, *55*, 340–352.

(50) Beaucage, G. Approximations Leading to a Unified Exponential/Power-Law Approach to Small-Angle Scattering. *J. Appl. Crystallogr.* **1995**, *28*, 717–728.

(51) Neburkova, J.; Vavra, J.; Cigler, P. Coating nanodiamonds with biocompatible shells for applications in biology and medicine. *Curr. Opin. Solid State Mater. Sci.* **2017**, *21*, 43–53.

(52) Tabachnikov, S. Dragon Curves Revisited. *Math Intelligencer* **2014**, *36*, 13–17.

(53) Hashimoto, T.; Amino, N.; Nishitsuji, S.; Takenaka, M. Hierarchically self-organized filler particles in polymers: cascade evolution of dissipative structures to ordered structures. *Polym. J.* **2019**, *51*, 109–130.

(54) Takenaka, M. Analysis of structures of rubber-filler systems with combined scattering methods. *Polym. J.* **2013**, *45*, 10–19.

(55) Koga, T.; Takenaka, M.; Aizawa, K.; Nakamura, M.; Hashimoto, T. Structure Factors of Dispersible Units of Carbon Black Filler in Rubbers. *Langmuir* **2005**, *21*, 11409–11413.

(56) Barnard, A. S.; Ōsawa, E. The impact of structural polydispersivity on the surface electrostatic potential of nanodiamond. *Nanoscale* **2014**, *6*, 1188–1194.